The Astrophysical Journal, 669:21–31, 2007 November 1

THE MASSES AND SHAPES OF DARK MATTER HALOS FROM GALAXY-GALAXY LENSING IN THE CFHT LEGACY SURVEY

Laura C. Parker
Department of Physics and Astronomy, University of Waterloo, Waterloo, ON N2L 3G1, Canada; and European Southern Observatory, Karl-Schwarzschild-Strasse 2, 85748 Garching, Germany

Henk Hoekstra
Department of Physics and Astronomy, University of Victoria, Victoria, BC V8W 2Y2, Canada

Michael J. Hudson
Department of Physics and Astronomy, University of Waterloo, Waterloo, ON N2L 3G1, Canada

Ludovic van Waerbeke
Department of Physics and Astronomy, University of British Columbia, Vancouver, BC V6T 1Z1, Canada

and

Yannick Mellier
Institut d'Astrophysique de Paris, 98bis, Boulevard Arago, 75014 Paris, France
Received 2006 August 8; accepted 2007 July 9

ABSTRACT

We present the first galaxy-galaxy weak-lensing results using early data from the Canada-France-Hawaii Telescope Legacy Survey (CFHTLS). These results are based on $\sim$22 deg^2 of i' data. From these data, we estimate the average velocity dispersion for an L_* galaxy at a redshift of 0.3 to be 137 ± 11 km s^{-1}, with a virial mass, M_{200}, of $(1.1 \pm 0.2) \times 10^{12}\ h^{-1}\ M_\odot$ and a rest-frame mass-to-light ratio of $173 \pm 34\ h\ M_\odot/L_{R_c,\odot}$. We also investigate various possible sources of systematic error in detail. In addition, we separate our lens sample into two subsamples, divided by apparent magnitude and thus average redshift. From these early data we do not detect significant evolution in galaxy dark matter halo mass-to-light ratios at redshifts from 0.45 to 0.27. Finally, we test for nonspherical galaxy dark matter halos. Our results favor a dark matter halo with an ellipticity of $\sim$0.3 at the 2 σ level when averaged over all galaxies. If the sample of foreground lens galaxies is selected to favor elliptical galaxies, the mean halo ellipticity and significance of this result increase.

Subject headings: dark matter — galaxies: halos — galaxies: fundamental parameters — gravitational lensing

1. INTRODUCTION

It is widely accepted that galaxies live in massive dark matter halos, but the properties of these halos are not particularly well understood. Dark matter halos around individual galaxies introduce small coherent distortions to the shapes of background galaxies. This signal, weak gravitational lensing, can be used to infer properties of foreground galaxy dark matter halos, such as their sizes and shapes (e.g., Brainerd et al. 1996; Hudson et al. 1998; Hoekstra et al. 2003; Sheldon et al. 2004; Hoekstra et al. 2004, 2005; Mandelbaum et al. 2006b; Heymans et al. 2006b). Galaxy-galaxy lensing also provides an important link between numerical simulations, which model the dark matter very well, and other observational techniques, which are restricted to studying the (likely) biased luminous matter. The ability to connect observed galaxies to the properties of their dark matter halos provides important insights into the details of galaxy formation. Galaxy-galaxy lensing can also be used to constrain alternative theories of gravity. If observations such as flat rotation curves are due to a modified gravity law, then the weak-lensing signal at large distances from the galaxy center should be isotropic. If an anisotropic galaxy-galaxy lensing signal is observed around galaxies, then this is a strong piece of evidence for flattened dark matter halos and disfavors any modified gravity theory (e.g., Mortlock & Turner 2001).

Other techniques with which to map the dark matter content of galaxies, including extended rotation curves and dynamical methods, require visible tracer populations and are thus capable of probing only the inner regions of galaxy halos. Using satellite galaxies to probe the potential wells of galaxies offers an interesting alternative (e.g., Zaritsky & White 1994; Prada et al. 2003; Conroy et al. 2005), but this technique requires the assumption of dynamical equilibrium and is susceptible to the inclusion of interlopers, which can bias the results.

The study of galaxy-galaxy lensing has grown dramatically since its first detection 10 years ago (Brainerd et al. 1996), largely due to improved analysis techniques and a wealth of wide-field data. The basic requirement for a weak-lensing measurement is wide-field imaging of reasonable depth and image quality. The most precise galaxy-galaxy lensing measurements to date are from the Red-Sequence Cluster Survey (RCS; Hoekstra et al. 2004) and the Sloan Digital Sky Survey (SDSS; Mandelbaum et al. 2006b), which are not particularly deep surveys, but cover enormous areas. Measurements have been made from space in small fields (e.g., Hudson et al. 1998) and from large ground-based observations (e.g., Sheldon et al. 2004; Hoekstra et al. 2004; Mandelbaum et al. 2006b).

In this study we examine the weak-lensing signal from a $\sim$22 deg^2 area of sky from two fields of the Wide component of the Canada-France-Hawaii Telescope Legacy Survey (CFHTLS).[1] These data represent a small fraction of the total CFHTLS Wide area that will be covered by the end of the survey in 2008 (approximately 170 deg^2). This early analysis is based on i' data only and therefore lacks color and redshift information for both the

[1] See http://www.cfht.hawaii.edu/Science/CFHLS/.

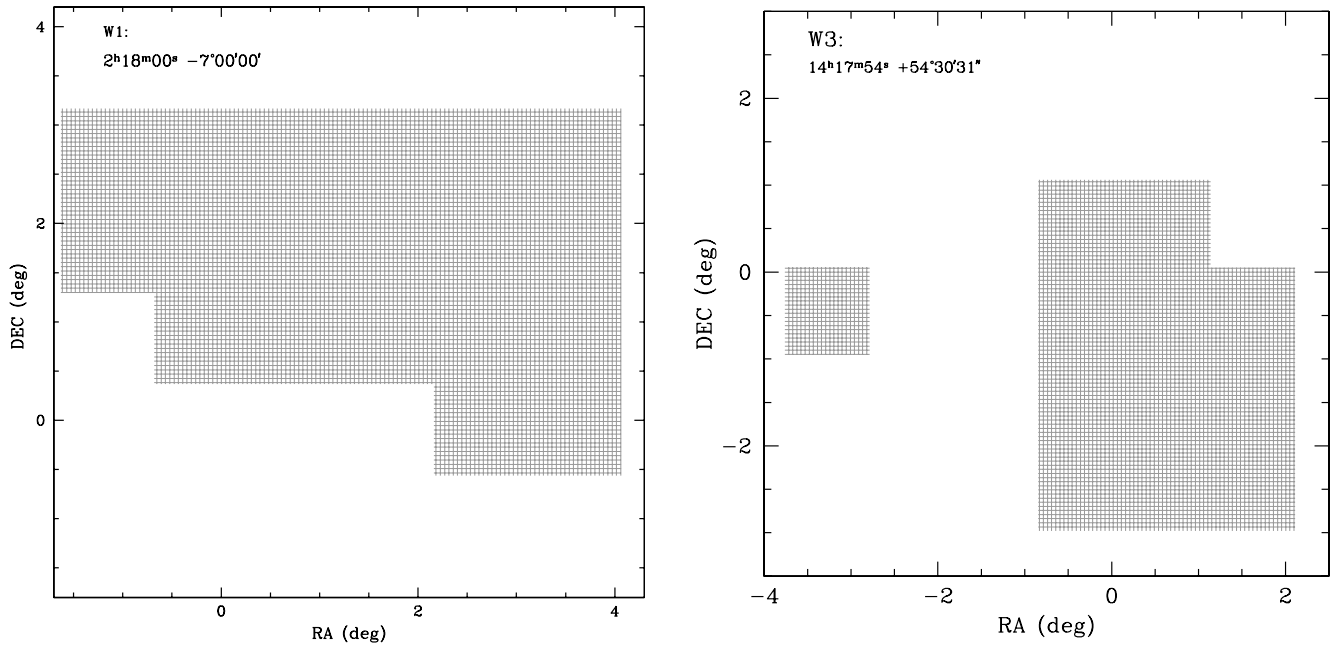

FIG. 1.—CFHTLS observations of the W1 and W3 fields. The effective area is approximately 22 deg^2 from 31 pointings (19 deg^2 in W1 and 12 deg^2 in W3). Bright stars and bad pixels are masked.

lenses and the sources. Compared to previous large surveys used for galaxy-galaxy lensing (e.g., Hoekstra et al. 2004; Sheldon et al. 2004), the CFHTLS is deeper, and therefore we have a higher source density and can probe galaxy halos at systematically higher redshifts.

In this paper we introduce the CFHTLS data (§ 2) and explain the redshift distribution determination and the galaxy shape measurements. In § 3 we show the first CFHTLS galaxy-galaxy lensing measurements, including the determination of the average halo velocity dispersion, as well as estimates for the average galaxy mass and mass-to-light (M/L) ratio. We also investigate a number of possible sources of systematic error. We conclude this section by dividing the lens sample into low- and high-redshift samples in order to look for evolution in the galaxy halos. In § 4 we present a measurement of the halo shapes using anisotropic weak lensing. In § 5 we summarize and discuss these results.

Throughout the paper, we assume a cosmology with $\Omega_m = 0.3$ and $\Omega_\Lambda = 0.7$. Results are presented in units of the Hubble parameter, h (the Hubble constant rescaled in units of 100 km s^{-1} Mpc^{-1}), which is assumed to be 1.

2. DATA

Canada and France have united to use a large fraction of their telescope time at the Canada-France-Hawaii Telescope (CFHT) to complete a 5 year photometric survey. The survey makes use of the new MegaCam instrument at CFHT. The camera is comprised of 36 separate CCD chips and produces distortion-corrected 1 deg^2 images with superb image quality. The survey is divided into Deep, Wide, and Very Wide components. The Wide component is primarily designed for weak-lensing studies. These data are well suited to the study of galaxy dark matter halos, as will be discussed in this paper, but also for the study of lensing by the large-scale mass distribution in the universe, cosmic shear (Hoekstra et al. 2006). Cosmic shear studies complement the Type Ia supernovae analysis from the CFHTLS Deep survey (Astier et al. 2006), since they can both be used to determine cosmological parameters, particularly the dark energy equation of state.

This galaxy-galaxy lensing project makes use of early data from the CFHTLS Wide survey. The Wide data will eventually cover ~170 deg^2 in five filters (u^*, g', r', i', and z'). The observations are divided into four large patches that are well separated in right ascension. Each patch is located far from the Galactic plane in order to minimize extinction and contamination from bright stars.

The early data used in this paper study are based on 31 pointings taken in the i' band and cover an effective area of roughly 22 deg^2. The data are from the W1 and W3 fields, which will total 72 and 49 deg^2, respectively, at the end of the survey. W1 is centered at R.A.(J2000.0) = $2^h18^m00^s$ and decl.(J2000.0) = $-7°00'00''$ and overlaps with the *XMM-Newton* Large-Scale Structure (XMM-LSS) field. W3 is centered at R.A.(J2000.0) = $14^h17^m54^s$ and decl.(J2000.0) = $+54°30'31''$ and overlaps with the Groth strip field. Figure 1 shows the coverage of the data used in this paper, totaling 19 deg^2 from W1 and 12 deg^2 from W3. The images are masked to avoid bright stars, diffraction spikes, and bad pixels. The source density is ~20 galaxies arcmin^{-2}. These data were obtained in the 2003B, 2004A, and 2004B observing semesters. The median seeing for the images used in this project is 0.76″; however, more recent CFHTLS observations have improved image quality. The image quality degrades toward the edge of the images, but only data with subarcsecond seeing are included in this analysis. More details on the data used in this analysis can be found in Hoekstra et al. (2006).

2.1. *Images and Catalogs*

The i' images used in this analysis are provided to the Canadian and French astronomical communities via the Canadian Astronomical Data Centre (CADC). The basic data reduction pipeline, Elixir, is used to provide flat-fielded, debiased images, as well as photometric zero points and an initial astrometric solution. The CFHTLS data are complicated by the fact that there are large dithers between some of the images. Therefore, some objects may appear on different chips in the individual exposures. This can lead to complicated PSF anisotropies, which are difficult to model and correct for. With this early analysis, all such "multichip" data are

excluded. Each chip is stacked separately with data only from that chip. This comes at a cost of losing approximately 20% of the area, but it ensures accurate PSF anisotropy correction. Using stacks for which all of the data comes from only one chip is a conservative approach, and, since the MegaCam PSF is smooth from chip to chip, future analyses will not impose this restriction. As described in Hoekstra et al. (2006), any images with poor seeing (>1″) are excluded from the stacks. In addition, the images are inspected by eye to mask out areas contaminated by bleeding stars, diffraction spikes, or other cosmetic defects. The stacks for these CFHTLS data were created using the SWarp routine.[2] The stacks are created from six or seven individual images of 620 s exposures; thus, each stack is >1 hr and reaches a depth of ∼25 in i'.

A critical aspect of weak-lensing measurements is accurately determining the shapes of faint objects. The ability to do this with stacked images requires very accurate astrometric solutions so that no spurious shape distortions are introduced in the stacking procedure. For this reason, it is necessary to improve on the basic astrometry from the Elixir-processed data and include higher order corrections. The images and catalogs used in this galaxy-galaxy lensing analysis are the same as those used in the first cosmic shear analysis of the CFHTLS Wide data (Hoekstra et al. 2006). The catalog details can be found in the shear paper, but we outline the major points briefly here.

The basic technique for correcting the image astrometry is as follows:

1. Retrieve a red image from the second-generation Digital Sky Survey (POS II) for each pointing.
2. Use SExtractor (Bertin & Arnouts 1996) to generate a large catalog of stars.
3. Match the astrometric catalog to each MegaCam image, averaging the positions of objects that appear on more than one chip (due to the large dither offsets).
4. Use this master catalog to generate an astrometric solution for each chip.

By following the above procedure, a stack can be created using all of the input images with the new astrometric solution applied. As was discussed above, the stacks were created for each chip individually and include only data from that chip, so that the PSF pattern could be corrected properly. This reduces the total area but simplifies the PSF corrections.

2.2. *Galaxy Shapes*

The carefully stacked i' images were processed with the peak-finding algorithm of Kaiser et al. (1995). Objects that were detected to be more than 5 σ above the sky background were added to the source catalog. The catalog is then cleaned to include only objects larger than the PSF (points to the right of the stellar locus, identified in a plot of magnitude vs. half-light radius, as in Hoekstra et al. 2002). These objects are then analyzed in more detail in order to determine their apparent i' magnitudes and half-light radii, as well as their shape parameters. The shape is defined by two polarization "vectors":

$$e_1 = \frac{Q_{11} - Q_{22}}{Q_{11} + Q_{22}}, \quad (1)$$

$$e_2 = \frac{2Q_{12}}{Q_{11} + Q_{22}}, \quad (2)$$

where Q_{ij} are weighted with a Gaussian function that scales with galaxy size.

[2] Available at http://terapix.iap.fr/rubrique.php?id_rubrique=49.

2.2.1. *Shape Corrections*

The measured shapes must be corrected for distortions such as the effects of seeing and PSF anisotropy. This is done by following the techniques outlined in Kaiser et al. (1995) and Hoekstra et al. (1998). A sample of stars is found in the images, and they are used to characterize the seeing and any anisotropy in the PSF. The shapes of the stars are fitted with a second-order polynomial for each chip in the CFHTLS stacks individually (i.e., the stars are fitted in the final stacked image, but each stacked chip is handled individually). The shapes of the stars are then used to correct the shapes of all of the galaxies. The catalogs include the position, magnitude, shape, error, and P^γ information, where P^γ is the pre-seeing shear polarizability and can be calculated from the images of stars and galaxies (Hoekstra et al. 1998).

The procedure outlined here to correct the galaxy shapes was recently tested in the Shear TEsting Program (Heymans et al. 2006a) and, with more realistic PSFs, in Massey et al. (2007). The results indicated that the procedure that was followed to create the catalogs in this analysis can reliably be used to measure weak shear to an accuracy within ∼2% of the true value. It is important to note that the morphologies in the Massey et al. (2007) and Heymans et al. (2006a) papers are simplified and do not consider possibilities, such as shear and noise, that vary as a function of position. The simulated images used in the Massey et al. (2007) analysis are based on the best available imaging from Suprime-Cam and thus do not have the identical signal-to-noise ratio or PSF size as the CFHTLS images; therefore, the quoted 2% shear accuracy should be taken as a rough estimate. However, the lack of B modes in the cosmic shear analysis using these catalogs (Hoekstra et al. 2006) is a powerful indicator that the level of systematics arising from PSF anisotropy is very small. Furthermore, galaxy-galaxy lensing is not very sensitive to PSF anisotropy, as we average over many pairs of galaxies that have random directions of PSF anisotropy.

2.3. *Redshift Distribution*

The final CFHTLS Wide data set will include photometric redshifts for every faint source, but at present we have only single-filter data available. For the analysis presented here, we select a sample of lenses and sources on the basis of their apparent i' magnitude. We define galaxies with $19 < i' < 22$ as lenses and galaxies with $22.5 < i' < 24.5$ as sources that are used to measure the lensing signal. The faint end of the source distribution is chosen to ensure high signal-to-noise ratio shape measurements and corresponds to the peak in the magnitude distribution (Fig. 2). This selection yields a sample of $\sim 2 \times 10^5$ lenses and $\sim 1.3 \times 10^6$ sources. These catalogs are used to generate 3.7×10^7 lens-source pairs within a projected radius of 2′ of the stacked lenses. All lens-source pairs within 7″ of the host galaxy are eliminated from the catalog, since their shape measurements are likely compromised by light from the host lens. The angular scale of 7″–2′ corresponds to a physical scale of ∼25–500 h^{-1} kpc at the median redshift of the lenses. Figure 2 shows the magnitude distribution for the entire sample of galaxies in the W1 and W3 fields used.

The lensing signal for an isothermal sphere is a function of $\langle\beta\rangle$, the average ratio of the angular diameter distances between the lens and source, D_{LS}, and between the observer and the source, D_S, as follows:

$$\beta = \max\left(0, \frac{D_{LS}}{D_S}\right). \quad (3)$$

Therefore, in order to interpret the detected shear measurements, it is necessary to know the redshifts of both the lenses and the

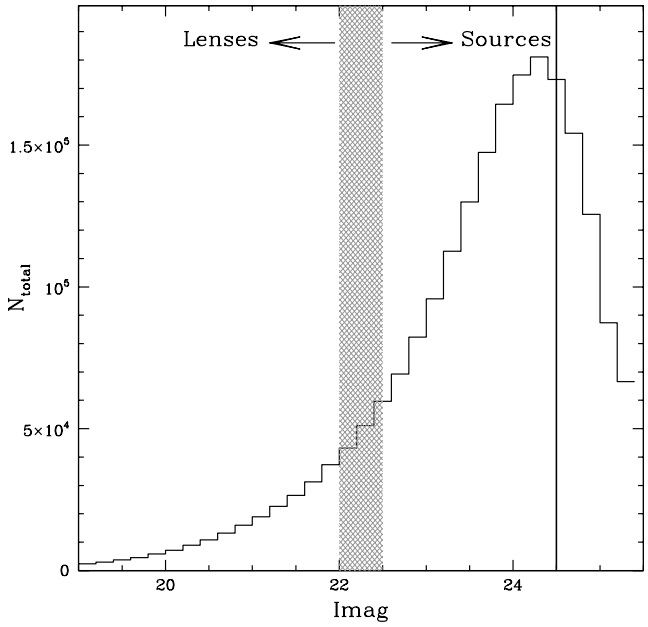

FIG. 2.—Lens and source magnitude distributions. This histogram shows the distribution of i' magnitudes for all galaxies in the W1 and W3 fields used in this analysis. The cross-hatched region divides the lenses and the sources, and the vertical line at $i' = 24.5$ shows the upper magnitude for the sources used.

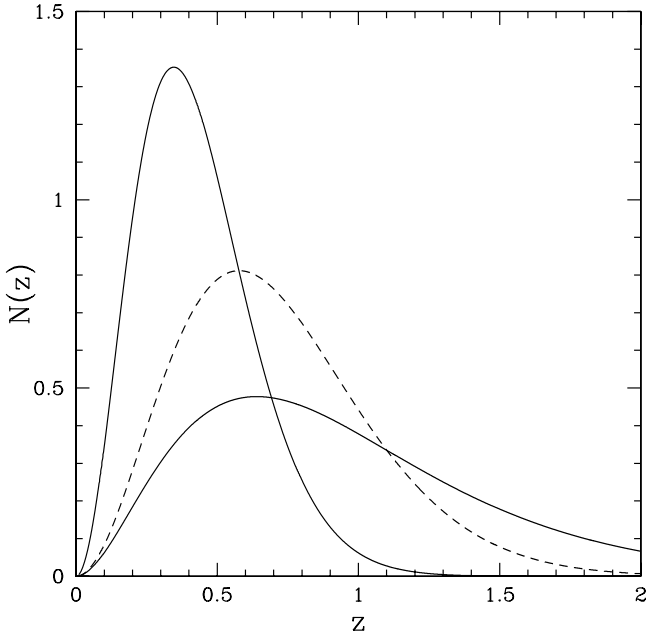

FIG. 3.—Plot of the $N(z)$ distribution. The lens and source distributions used in this analysis are shown with the solid lines. The sources have a median redshift of $\sim$0.9 and the lenses have a median redshift of $\sim$0.4. The dashed line shows the redshift distribution of the sources based on the photometric redshifts from the HDFs (Fernández-Soto et al. 1999). The sources are at lower redshifts using the HDF photometric redshifts, but the value of $\langle\beta\rangle$ is only $\sim$5% smaller.

sources. If the precise redshifts are not known for each object, then at least their distributions must be understood in order to convert shear measurements into physical properties such as velocity dispersions and halo masses. The CFHTLS data used here were taken in a single band, and so the redshift distributions of the sources and lenses must be estimated. The shear can only be estimated in projected angular bins and not in physical units such as kiloparsecs. Therefore, the lensing signal for a distant galaxy is measured on a much larger physical scale than that of a closer galaxy. The mixing of scales complicates the interpretation of the results, but we can still learn about the average properties of halos.

The lens catalogs contain relatively bright galaxies, and therefore the distribution of the redshifts is quite well understood from previous studies, such as the CNOC2 field galaxy survey (Yee et al. 2000). It is much more difficult to estimate the redshifts of faint sources, since they are generally too faint for spectroscopic redshift determination. The redshifts of faint galaxies are generally estimated using photometric redshifts. A spectroscopic study of the Hubble Deep Field (HDF) to depths of $\sim$24 in R_c showed that the spectroscopic redshifts agreed well with the photometric redshifts (Cohen et al. 2000).

The source and lens redshift distributions used in this analysis can be seen in Figure 3. The median lens redshift is $\sim$0.4, and the median source redshift is $\sim$0.9. The $N(z)$ distribution for the lenses was estimated using the functional form of Brown et al. (2003), which is based on COMBO-17 data. The COMBO-17 survey uses a combination of 17 wide- and narrowband filters to measure very accurate photometric redshifts in a 1 deg^2 patch:

$$\frac{dN}{dz} \propto \frac{z^2}{z_*^3} \exp\left[-\left(\frac{z}{z_*}\right)^{1.5}\right], \tag{4}$$

where z_* is related to the median redshift of the distribution by $z_* = z_m/1.412$ and z_m is a function of the apparent magnitude.

The source redshift distribution used in the analysis was estimated from photometric redshifts in the CFHTLS Deep fields (Ilbert et al. 2006). The functional form of the $N(z)_{\rm sources}$ is as follows:

$$N(z)_{\rm sources} = r_{\rm norm}\left(\frac{z}{z_0}\right)^{\lambda} \exp\left[-\left(\frac{z}{z_0}\right)^{\omega}\right], \tag{5}$$

$$r_{\rm norm} = \frac{\omega}{z_0 \Gamma[(1+\lambda)/\omega]}. \tag{6}$$

The values for λ, ω, and z_0 were calculated using the magnitude cuts of our source catalogs applied to the Ilbert et al. (2006) data.

The $N(z)$ distributions can then be used to estimate the angular diameter distances to the lenses and sources. If we assume a standard ΛCDM cosmology, this results in a value of $\langle\beta\rangle$ of 0.49. If we alternatively used a source distribution based on the Hubble Deep Fields North and South (Fernández-Soto et al. 1999), then we find a value of $\langle\beta\rangle$ of 0.46 ± 0.02, where the error is from the field-to-field variations in the HDFs and the finite number of galaxies. The β-value estimates are weighted in the same manner as the shear estimates, as will be discussed in the next section. The difference in source redshift distributions between the CFHTLS Deep fields and the HDFs is obvious in Figure 3. The sources are at slightly higher redshifts when using the CFHTLS photometric redshifts than with the distribution estimated from the HDF. The visible discrepancy between the photometric redshift distributions from the CFHTLS and the distributions based on the HDF is not statistically significant when one accounts for uncertainties in photometric redshift distributions due to cosmic variance affecting small fields (see Fig. 1 of van Waerbeke et al. [2006] for a dramatic illustration of this in the HDF). The different redshift distributions only change the $\langle\beta\rangle$-value by $\sim$5%.

3. ANALYSIS

The tangential shear signal must be fitted with an assumed halo mass model in order to extract physical properties of the halo, such

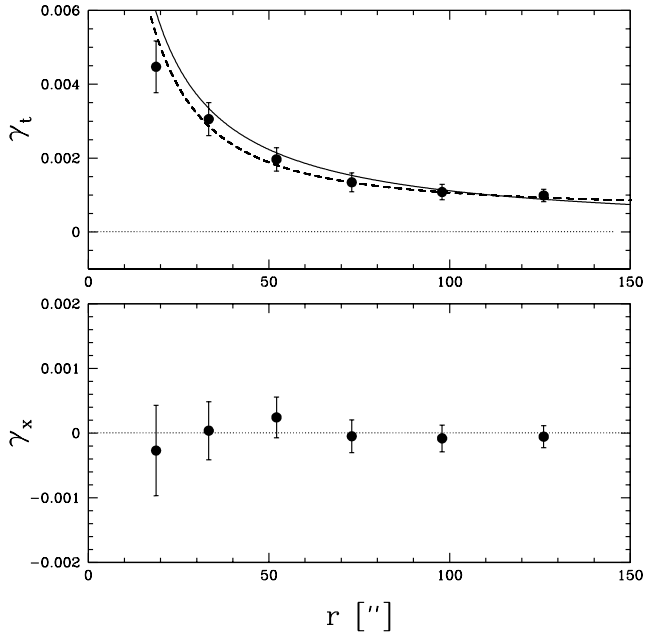

FIG. 4.—*Top*: Ensemble-averaged tangential shear as a function of radius around a sample of CFHTLS galaxies with $19 \lesssim i' \lesssim 22$. The best-fit isothermal sphere, shown with the solid line, yields an Einstein radius of $0.247'' \pm 0.020''$, corresponding to a velocity dispersion of $132 \pm 10\,\mathrm{km\,s^{-1}}$. The dashed line represents the best-fit NFW profile, corresponding to a halo with an r_{200} of 150 h^{-1} kpc. *Bottom*: Signal when the source images are rotated by 45°. Note the difference in scales between the top and bottom panels. No signal is present, as is expected if the signal in the top panel is due to gravitational lensing.

as velocity dispersion and mass. A common mass model assumed is the isothermal sphere, for which the tangential shear is proportional to the Einstein radius and hence to the velocity dispersion squared:

$$\theta_{\mathrm{E}} = \frac{4\pi\sigma^2}{c^2}\beta = \left(\frac{\sigma}{186\ \mathrm{km\ s^{-1}}}\right)^2 \beta\ \mathrm{arcsec}, \tag{7}$$

$$\gamma_t = \frac{\theta_{\mathrm{E}}}{2\theta} = \frac{2\pi\sigma^2}{c^2\theta}\beta. \tag{8}$$

In this study the lenses are stacked together, and the sources that lie within a projected radius of 2′ are divided into angular bins. The component of their shape tangential to the lens center is determined and averaged in each bin. Each shear calculation is weighted by the error in the shape measurement as described in Hoekstra et al. (2000). Galaxy-galaxy lensing measurements also have a convenient built-in systematic test. If the tangential lensing signal detected is due to gravity, then it should vanish if the source images are rotated by 45°. The tangential shear and "cross-shear" for the entire sample are plotted in Figure 4. The best-fit isothermal sphere has an Einstein radius of $0.247'' \pm 0.020''$. A lensing signal is detected at high significance (>12 σ). The cross-shear measurement is consistent with 0, as expected, and therefore the tangential shear signal is interpreted as being caused by weak lensing from an isothermal sphere potential.

The tangential shear measurements can also be fitted with other dark matter profiles, such as the Navarro-Frenk-White (NFW) profile (Navarro et al. 1996), given by

$$\rho(r) = \frac{\delta_c \rho_c}{(r/r_s)(1 + r/r_s)^2}, \tag{9}$$

where ρ_c is the critical density for closure of the universe. The scale radius, r_s, is defined as r_{200}/c_{NFW}, where c_{NFW} is the dimensionless concentration parameter, and δ_c is the characteristic overdensity of the halo. The tangential shear equations for a NFW halo can be found in Bartelmann (1996) and Wright & Brainerd (2000). The NFW density profile has two free parameters, but in this analysis we consider the concentration parameter to be fixed, obeying the relation between virial mass and concentration found in simulations by Bullock et al. (2001). The best-fit NFW profile, corresponding to a halo with a value of r_{200} of 0.15 h^{-1} Mpc (and therefore a value of M_{200} of $7.6 \times 10^{11}\ h^{-1}\ M_\odot$), is shown with the dashed line in the top panel of Figure 4.

3.1. *Systematics*

In order to verify the validity of our shear signal, we have performed a number of systematic tests. At the outset, we are confident that the catalog used in this analysis is free of major systematics because there were no significant B modes found in the cosmic shear analysis using the same catalog (Hoekstra et al. 2006). The initial systematic test is to calculate the cross-shear, as discussed above. We have also considered the fact that some lenses and sources are physically associated. We can estimate the level of this association by calculating the number density of galaxies in each bin, which decreases with radius. We have estimated the fractional excess of background sources around lenses, f_{bg}, and increased the shear signal by $1 + f_{\mathrm{bg}}$ to compensate. The background density of sources was estimated by counting the number of sources in bins around random lens positions. The random lens catalog was the same size as the lens sample used in this analysis. Our best-fit value of $f_{\mathrm{bg}} = 0.82r^{-0.63}$, where r is the radius in units of arcseconds, is similar to what has been found in previous measurements (e.g., Hoekstra et al. 2004). The fractional excess is a strong function of radius, and thus only the inner angular bins are influenced by physically associated lens-source pairs. This correction has been applied to all quoted values in this paper (e.g., θ_{E}, σ) and was calculated for each lens sample separately.

A further test of the signal can be made by measuring the tangential shear and cross-shear around random points in the field. The results from performing this test are demonstrated in Figure 5 and are consistent with no detected signal, as expected. The same number of random points as of foreground lens galaxies was used.

It is also important to examine the influence of intrinsic alignments. Without redshift information for our lenses and sources, it is possible that physically associated lens-source pairs are included in the analysis. If these pairs are aligned, then the tangential shear signal will be contaminated. Recent evidence has suggested that satellite galaxies' major axes preferentially point toward their host galaxies (Agustsson & Brainerd 2006b), which would decrease the galaxy-galaxy lensing signal. If we adopt the most pessimistic view and consider a very large contamination in the inner 250 kpc due to intrinsic alignment, we can compensate by boosting the tangential shear signal. If we apply a 40% boost to the inner three bins in Figure 4 (corresponding to roughly 250 kpc at the redshift of our lenses), adopting the worst case from Agustsson & Brainerd (2006a; 25%–40% suppression of shear on scales less than 250 kpc), then the best-fit isothermal sphere yields an Einstein radius that is 7% larger than that quoted above. This small difference is due to the fact that the outer three data points, with smaller error bars, constrain the isothermal sphere fit much more than do the three inner bins. This is an upper limit on the contamination from intrinsically aligned satellites.

Alternatively, we can also estimate the influence of intrinsic alignment by repeating the analysis after dividing the distant

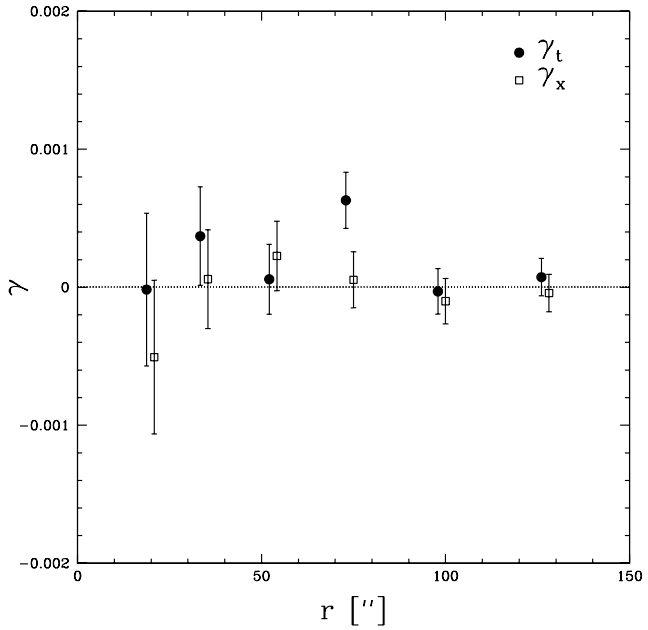

FIG. 5.—Ensemble-averaged tangential shear (*circles*) and cross-shear (*squares*) as a function of radius around a sample of random points in the CFHTLS fields. Both the signals are consistent with zero, as expected. Note that the cross-shear points have been slightly shifted so that the error bars are clearly visible.

sources into two subsamples on the basis of their apparent magnitudes, while keeping the lens sample identical. After rescaling by the new β-values, the shear signal should be the same, since the lens sample has not changed. If, however, there is significant intrinsic alignment, then the signal from the brighter sources (lower redshift) will be suppressed. We have carried out this test and found that the velocity dispersion derived from the shear signal computed using the brighter sources is indeed suppressed by $\lesssim$10%. The suppression due to intrinsic alignments for the entire sample would therefore be $<$10%. We have not applied any correction for intrinsically aligned sources; instead, we include this as part of our total systematic error budget.

One final potential systematic that should be discussed is possible contamination from stellar objects in the final source catalog. Moderately bright stars are easily identified, as they lie in a tight vertical locus in a plot of magnitude versus size. Bright stars saturate, and their measured sizes increase, but they can also be easily removed from the catalogs. There is some overlap between faint stars and galaxies, which can dilute the shear signal, but by extrapolating the number counts of stars to faint magnitudes, it is clear that stars will contribute at most a few percent to the total number counts. In addition, we consider only sources larger than the stellar PSF, which cleanly separates stars and galaxies to $i' \sim 24$ (Hoekstra et al. 2002). Furthermore, in this analysis we downweight faint sources, which significantly reduces the contamination from stars (Heymans et al. 2006a). The weight for sources fainter than $i' = 24$ is very low; thus, the level of stellar contamination is estimated to be $<$1%. It is important to note for the discussion of halo shapes below that this potential source of systematic error is irrelevant, as the stars are randomly distributed and the measurement is a relative one.

On the basis of the above considerations, we estimate that the total systematic error in our measurements is at most 10% (1 σ level). The exact level of possible systematic errors is difficult to estimate, as the error distributions for the various systematics are not known. Throughout the paper, the quoted errors are always statistical errors derived on the basis of the errors in the shape measurements and the number of sources in each bin.

3.2. *Velocity Dispersion*

The best-fit isothermal sphere yields a velocity dispersion of 132 ± 10 km s^{-1} (eqs. [7] and [8]). This measurement takes into account the fact that some lenses and sources will be physically associated. We can estimate the level of this association by calculating the number density of galaxies in each bin, which decreases with radius.

The velocity dispersion depends on the sample of lenses used and must be scaled in order to be compared to other results. This can easily be done by assuming the following scaling relation between luminosity and velocity dispersion:

$$\frac{\sigma}{\sigma_*} = \left(\frac{L}{L_*}\right)^{1/\alpha}, \tag{10}$$

where σ_* is the velocity dispersion of an L_* galaxy. The scaling factor α is generally assumed to be 3 or 4, motivated by the observations of the Faber-Jackson relation (Faber & Jackson 1976), for example. We based our L_* galaxy on the CNOC2 luminosity function results (Lin et al. 1999). Lin et al. measure L_* at $z = 0.3$, which after correction to the ΛCDM cosmology assumed here gives $1.3 \times 10^{10}\ h^{-2}\ L_{R_c,\odot}$. We used the color and k-corrections from Frei & Gunn (1994) to convert our magnitudes to R_c and evaluate the luminosity of our lenses. All luminosities are calculated with the assumption of the proportion of early and late types of galaxies found in the CNOC2 redshift survey, since the redshifts and brightnesses of the two samples are comparable (28% early types, 24% intermediate types, and 47% late types). It is also important to note that the average luminosity is calculated using the same weights used in the shear analysis.

The Einstein radius for an L_* galaxy is given by

$$\theta_{\rm E} = \frac{4\pi}{c^2}\frac{\sigma_*^2}{L_*^{2/\alpha}}\langle \beta L^{2/\alpha}\rangle, \tag{11}$$

where $\theta_{\rm E}$ is in units of radians. We estimate the average luminosity for our lens galaxies to be $\langle L\rangle = 1.1 \times 10^{10}\ h^{-2}\ L_{R_c,\odot}$. The scaled velocity dispersion can now be estimated for different assumed α-values. The results of scaling the observed velocity dispersion for our sample of lenses to a typical L_* galaxy are summarized in Table 1.

Note that, in principle, the tangential shear signal is due not only to the lens galaxy in question (the one-halo term, which assumes that the galaxies are central galaxies), but also to other masses clustered with the primary galaxy (the two-halo term). In practice, however, the velocity dispersion is estimated from the best-fit isothermal sphere out to a radius of $\sim$130″, which at these redshifts corresponds to a physical scale of much less than 1 h^{-1} Mpc and thus should still be dominated by the one-halo term (Zehavi et al. 2004). This is not strictly true for satellite galaxies, for which the contribution to the lensing signal from the host halo would kick in on smaller scales (Yoo et al. 2006). However, as the shear profile is well fitted by both singular isothermal sphere and NFW profiles, this is not a significant concern.

A galaxy-galaxy lensing analysis of the COMBO-17 data by Kleinheinrich et al. (2005) estimated the value for σ_* for various scenarios, including those in which the redshift is known for every lens and every source and those for which there is no redshift information available. The latter case can be compared with our results. They obtained a mean value of σ_* of 156^{+24}_{-30} km s^{-1}.

TABLE 1
PROPERTIES FOR THE VARIOUS LENS SAMPLES

Sample	$\langle z \rangle$	$\langle \beta \rangle$	$\langle L \rangle$ ($10^{10}\ h^{-2}\ L_{R_c,\odot}$)	$\langle \sigma^2 \rangle^{1/2}$ (km s^{-1})	α	σ_* (km s^{-1})	$M_{\rm tot}$ ($10^{12}\ h^{-1}\ M_\odot$)	M_{200} ($10^{12}\ h^{-1}\ M_\odot$)	M/L_* ($h\ M_\odot/L_{R_c,\odot}$)
Full	0.35	0.49	1.11	132 ± 10	4	137 ± 11	2.2 ± 0.4	1.1 ± 0.2	173 ± 34
	0.35	0.49	1.11	132 ± 10	3	141 ± 12	2.4 ± 0.5	1.2 ± 0.2	189 ± 37
Faint	0.45	0.44	1.07	129 ± 11	4	134 ± 12	2.1 ± 0.5	01.0 ± 0.2	165 ± 43
	0.45	0.44	1.07	129 ± 11	3	137 ± 12	2.1 ± 0.5	1.1 ± 0.2	174 ± 46
Bright	0.27	0.67	1.26	141 ± 18	4	142 ± 18	2.7 ± 0.6	1.2 ± 0.3	206 ± 54
	0.27	0.67	1.26	141 ± 18	3	142 ± 18	2.7 ± 0.4	1.2 ± 0.3	206 ± 54

NOTE.—The quoted errors do not include mass model uncertainties.

Hoekstra et al. (2005) used data from the RCS to estimate the properties of galaxy dark matter halos using galaxy-galaxy lensing without redshift information. They found a value for σ_* of 136 ± 8 km s^{-1}. It is important to note that the estimate for L_* is slightly different in each of these studies, but the results agree within the errors.

3.3. *Halo Masses*

The total extent and mass of dark matter halos can be estimated by assuming a mass model for the galaxy halos as suggested by Brainerd et al. (1996) with a density profile of

$$\rho(r) = \frac{\sigma^2 s^2}{2\pi G r^2 (r^2 + s^2)}, \tag{12}$$

where s is a measure of the truncation scale of the halo. This profile is an isothermal sphere at small radii with a cutoff at large radii, characterized by the scale s, which scales with velocity dispersion (Schneider & Rix 1997) as

$$s = s_* \left(\frac{\sigma}{\sigma_*} \right)^2. \tag{13}$$

If we assume this truncated isothermal sphere halo model, the mass enclosed within a sphere of radius r is

$$M(r) = \frac{2\sigma^2 s}{G} \arctan(r/s), \tag{14}$$

which, because of the truncation, results in a finite mass (Hoekstra et al. 2004) of

$$M_{\rm tot} = \frac{\pi \sigma^2 s}{G} = \left(7.3 \times 10^{12}\ h^{-1}\ M_\odot\right) \left(\frac{\sigma}{100\ \text{km s}^{-1}} \right)^2 \frac{s}{1\ \text{Mpc}}. \tag{15}$$

The truncation scale can be assumed to be constant for all halos, in which case the M/L ratio would be $\propto L^{1/2}$, if $L \propto \sigma^4$. This is the favored model in recent analyses (e.g., Guzik & Seljak 2001; Hoekstra et al. 2005). Alternatively, it can be assumed that the M/L ratio is constant for all galaxy halos, in which case $s \propto \sigma^2$ (Brainerd et al. 1996; Hudson et al. 1998). We do not explore the various possible M/L ratio scalings in this paper, as we assume a value for the truncation radius from the literature and do not directly fit a truncated isothermal sphere model.

Assuming the truncation radius found by Hoekstra et al. (2004) for an L_* galaxy of 185 ± 30 kpc, we estimate the total mass of our L_* galaxy to be $(2.2 \pm 0.4) \times 10^{12}\ h^{-1}\ M_\odot$ if $L \propto \sigma^4$ and $(2.4 \pm 0.5) \times 10^{12}\ h^{-1}\ M_\odot$ if $L \propto \sigma^3$. The results are in good agreement with the results from the RCS (Hoekstra et al. 2004), which found the total halo mass to be $(2.7 \pm 0.6) \times 10^{12}\ h^{-1}\ M_\odot$. We estimate the virial mass, M_{200}, of our galaxy halos, assuming an isothermal sphere model, to be $(1.1 \pm 0.2) \times 10^{12}\ h^{-1}\ M_\odot$, where M_{200} is the mass inside the virial radius r_{200}, defined as the radius where the mass density is 200 times the critical density. This is in good agreement with the results from the RCS, where the virial mass of L_* halos was estimated at $(11.7 \pm 1.7) \times 10^{11}\ h^{-1}\ M_\odot$ (Hoekstra et al. 2005). Our results are also in good agreement with results from the lower redshift SDSS sample, where the virial mass of an L_* halo was found to be $13.2^{+6.0}_{-5.6} \times 10^{11}\ h^{-1}\ M_\odot$ (Mandelbaum et al. 2006b). In order to make this comparison, we chose the central virial mass found for $\langle L/L_* \rangle = 1.1$ (see Table 3 of Mandelbaum et al. 2006b) and scaled this to L_*. We then scaled the SDSS from an NFW profile with a virial radius defined using $\rho = 180\bar{\rho}$ to a singular isothermal sphere profile with a virial radius defined by $\rho = 200\rho_{\rm crit}$. The GEMS team has estimated the virial mass of halos for a sample at higher redshift (Heymans et al. 2006b). They estimate that the virial mass for an L_* galaxy at a redshift of $\sim$0.65 is $14.1^{+3.7}_{-4.5} \times 10^{11}\ h^{-1}\ M_\odot$. For this comparison we once again transformed from an NFW profile to a singular isothermal sphere profile for an L_* galaxy, using our definition of the virial radius. Our measured velocity dispersion for an L_* galaxy is also in agreement with results from fundamental plane measurements (Sheth et al. 2003).

We can use the luminosity of an L_* galaxy together with the mass estimates above in order to calculate a typical M/L ratio. This leads to a M/L ratio for an L_* galaxy of $173 \pm 34\ h\ M_\odot/L_{R_c,\odot}$, if we assume that $\alpha = 4$.

3.4. *Evidence for Evolution?*

The CFHTLS data are ideally suited to looking for evolution in dark matter halos with redshift. The high signal-to-noise ratio of our primary result permits the division of the lenses into subsamples at different redshifts. With these early data there is a sufficient signal-to-noise ratio to divide the foreground lens samples into multiple bins; however, without redshift or color information, this proves difficult. Nevertheless, as was indicated earlier, we can divide the lenses on the basis of their observed i' magnitudes. The brighter lenses will be on average at a lower redshift, while faint lenses will be, on average, at a higher redshift. We decided to apply a magnitude cut at 20.5 in i'. This leads to a "bright lens sample" containing $\sim 4 \times 10^4$ galaxies and a "faint lens sample" containing $\sim 1.5 \times 10^5$ galaxies. This selection results in a low-redshift sample with a median redshift of 0.27 and a high-redshift sample with a median redshift of 0.45.

We repeated the tangential shear analysis described in the previous section (§ 3), and the results are shown in Figure 6. There is a striking difference in the tangential shear profiles for the two lens subsamples. However, as indicated in equation (7), the velocity

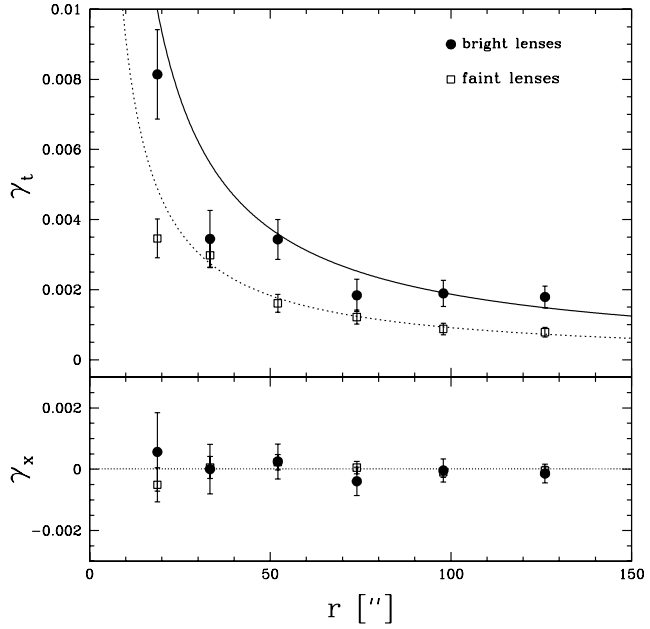

FIG. 6.—*Top*: Tangential shear signal for two samples of foreground lenses. *Bottom*: Cross-shear signal when the source images are rotated by 45°. The faint lenses (*squares*) have $i' > 20.5$, while the bright lenses (*circles*) have $i' < 20.5$.

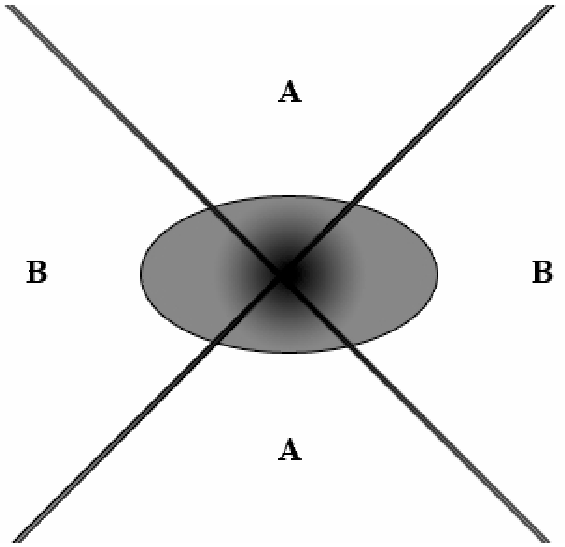

FIG. 7.—Schematic of anisotropic shear. If galaxy halos are not spherical, then there should be a difference in the tangential shear signal coming from the regions labeled with an "A" versus those labeled with a "B."

dispersion is also dependent on the parameter β. The source catalogs used are the same as those used in the analysis of the entire sample, and therefore so is the source redshift distribution. However, these two samples of lenses have very different redshift distributions, and thus their average β-values will also be different. The faint lens population has $\langle\beta\rangle = 0.44$, while $\langle\beta\rangle = 0.67$ for the bright lenses.

The differences in β can explain most of the offset between the two shear profiles in Figure 6; however, it is still interesting to scale the velocity dispersions to those of a typical L_* galaxy to see if any real difference can be seen in the dark matter halos of the two lens samples. The results are shown in Table 1. We do not see conclusive evidence for evolution in galaxy dark matter halos in this redshift range, but this is not so surprising, due to the lack of photometric or spectroscopic redshift information with which to clearly divide the lens populations.

4. HALO SHAPES

An important insight into the nature of dark matter comes from the shapes of dark matter halos. Dynamical measurements can be used to trace out the halo shapes on small scales, but they cannot be used on larger scales where there are no visible tracers. Numerical simulations of CDM indicate that dark matter halos should be flattened and more often prolate than oblate (Dubinski & Carlberg 1991; Springel et al. 2004; Allgood et al. 2006). Simulations of self-interacting dark matter produce more spherical halos (Davé et al. 2001).

Alternative theories of gravity, such as modified Newtonian dynamics (MOND; Milgrom 2002), attempt to explain astrophysical observations by modifying gravity rather than invoking nonbaryonic dark matter. Nonrelativistic theories of modified gravity cannot provide predictions for lensing measurements and therefore cannot be tested by lensing observations. However, there is now a candidate relativistic modified gravity theory, as presented by Bekenstein (2004), that can be used as an alternative to dark matter to explain relativistic phenomena such as lensing. Thus far, this theory appears to match many observations (Skordis et al. 2006; Zhao et al. 2006). One interesting test for this theory is the inferred shapes of galaxy dark matter halos from weak lensing (e.g., Mortlock & Turner 2001).

Modified gravity theories predict that the lensing signal is due to the observed luminous material, and thus any anisotropy in the lensing measurement is due to the anisotropy in the distribution of gas and stars. Therefore, on small scales one would expect the lensing signal to be anisotropic, since galaxies themselves are, but on the large scales probed by galaxy-galaxy lensing, one would expect a nearly isotropic signal, since there is no luminous material present at large radii from the galaxy center (provided that the galaxy is isolated and not in a group or cluster). If a highly anisotropic signal is detected at large radii, this provides an interesting constraint on modified gravity theories and provides supporting evidence for dark matter theories. The predictions from MOND of spherical halos assumes that the lens galaxies are isolated, and not in groups or clusters where there could be light contamination on large scales.

Galaxy-galaxy lensing measurements have generally assumed that dark matter halos are spherical, but a recent galaxy-galaxy measurement by Hoekstra et al. (2004) detected a significant flattening of dark matter halos. This result was not observed in the latest analysis of SDSS data by Mandelbaum et al. (2006a). However, Mandelbaum et al. did find marginal evidence for flattened halos when they restricted their lens sample to red galaxies.

One important note is that all such measurements rely on the assumption that the mass distribution of the halo is aligned with the light distribution of the galaxy. If the halo flattening is not correlated with the light profile orientation, then this simple measurement is much more difficult to interpret, and the flattening signal is likely systematically suppressed.

Anisotropic galaxy-galaxy lensing can be used to measure the shapes of dark matter halos (Brainerd & Wright 2000; Natarajan & Refregier 2000). One simple approach to try to detect if galaxy dark matter halos are nonspherical is to test whether the tangential shear signal is different along the semimajor and semiminor axes of the visible galaxy (Brainerd & Wright 2000).

The analysis described in the previous section (§ 3) was repeated for the galaxy lenses, this time dividing the sources into those within 45° of the semiminor axis and those within 45° of the semimajor axis (see the schematic in Fig. 7). The tangential shear results can be seen in Figure 8. The signal from the two angular

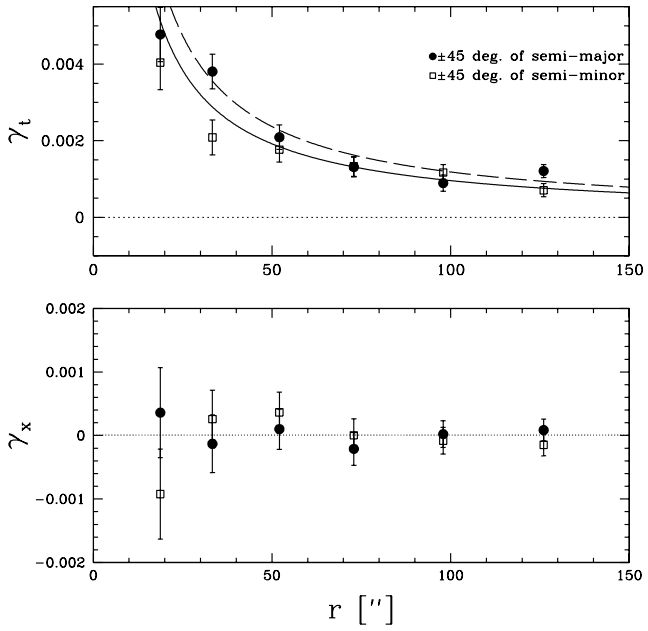

FIG. 8.—Mean tangential shear (*top*) for sources close to the semimajor axes (*circles*) and the semiminor axes (*squares*). The best-fit isothermal sphere for the sources within 45° of the semimajor axes, as indicated by the dashed line, yields an Einstein radius of $0.270'' \pm 0.031''$, corresponding to a velocity dispersion of 138 ± 15 km s^{-1}. The best-fit isothermal sphere for the sources within 45° of the semiminor axes, as indicated by the solid line, yields an Einstein radius of $0.211'' \pm 0.021''$, corresponding to a velocity dispersion of 122 ± 12 km s^{-1}. The cross-shear (*bottom*) is consistent with 0, as expected.

bins of sources is very similar. The best-fit isothermal spheres yield Einstein radii of $0.211'' \pm 0.021''$ and $0.270'' \pm 0.031''$, corresponding to velocity dispersions of 122 ± 12 and 138 ± 15 km s^{-1}, respectively.

We calculated the ratio of $\langle\gamma\rangle_{\rm minor}$ to $\langle\gamma\rangle_{\rm major}$ out to 70″ (which corresponds to $\sim$250 h^{-1} kpc, for comparison to Brainerd & Wright 2000), and the results are plotted in Figure 9. The best-fit

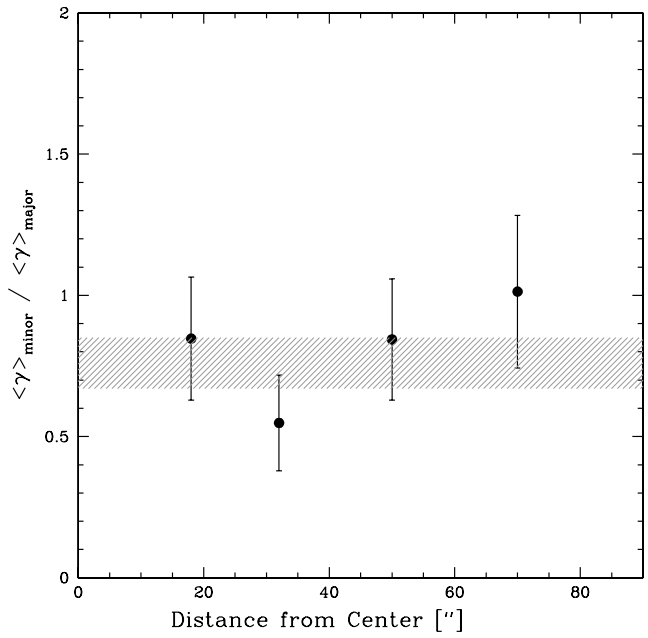

FIG. 9.—Ratio of mean shear experienced by sources closest to the minor axes of a foreground lens to that experienced by sources closest to the major axes. The weighted average shear ratio is 0.76 ± 0.10, favoring a halo with an ellipticity of 0.3.

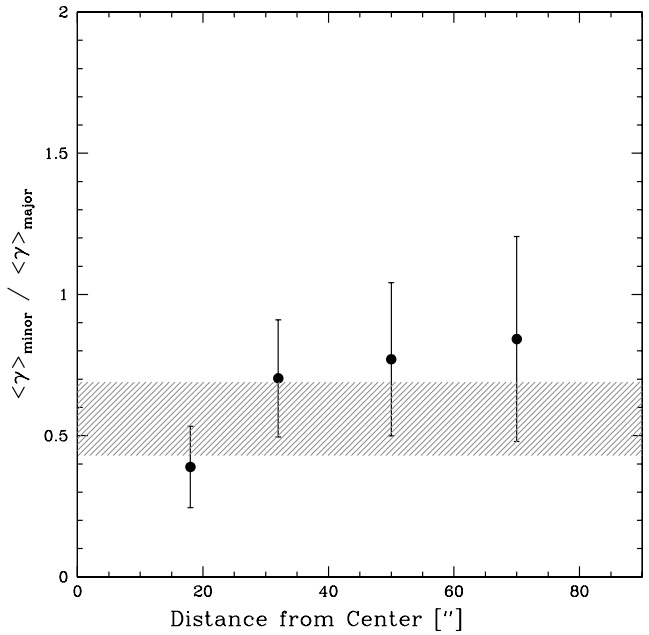

FIG. 10.—Same as Fig. 9, but with the roundest lenses ($e < 0.15$) excluded. Lenses that appear circular on the sky have more poorly determined semimajor axis positions and therefore have been excluded from this plot. The weighted average shear ratio is 0.56 ± 0.13.

shear ratio is 0.76 ± 0.10, indicating a $\sim 2\,\sigma$ detection of nonsphericity for dark matter halos. Examination of the minor axis–to–major axis shear ratio as a function of radius in Figure 1 of Brainerd & Wright (2000) suggests that a ratio of 0.76 corresponds to a halo ellipticity of $\sim$0.3.

It is important to measure the anisotropic weak-lensing signal for a sample of well-understood lenses. A way to improve the measurement of anisotropic weak lensing is to select a sample of lenses with a well-defined semimajor axis direction. Therefore, it is perhaps prudent to choose only the brighter lenses, or to discard those galaxies with noisy shape measurements or with very little ellipticity. If a lens has an extremely small measured ellipticity, then determining an accurate semimajor axis location is very difficult and prone to errors. We choose to repeat the anisotropic weak-lensing signal for all lenses with an ellipticity of >0.15, which corresponds to an axis ratio of <0.8. The results are shown in Figure 10. The best-fit shear ratio is 0.56 ± 0.13, which, according to Brainerd & Wright (2000), favors a halo model with an ellipticity of $\sim$0.5, although directly comparing to Brainerd & Wright is not strictly correct, as their results are based on simulations including the full distribution of galaxy shapes.

In addition, it is of interest to divide the lens population into red and blue (or early- and late-type) subsamples and to focus mainly on the early-type galaxies, since they will not be so susceptible to inclination effects (Novak et al. 2006). Without color or morphology information, this was a difficult task with our data, but by selecting a sample of galaxies with an axis ratio, b/a, between 0.5 and 0.8, we are selecting mostly early-type galaxies (Alam & Ryden 2002). The results from applying this cut in axis ratio to our lenses are shown in Figure 11. Using preferentially early-type galaxies yields a shear ratio of 0.61 ± 0.14. This favors a halo with an ellipticity of $\sim$0.4 and represents a more significant detection of nonspherical halos than when using the entire lens sample. It is important to note that in this analysis we make the assumption that the galaxies we are using are isolated, so a comparison to MOND is perhaps not completely justified. However, the lensing signal in this analysis is measured on scales dominated

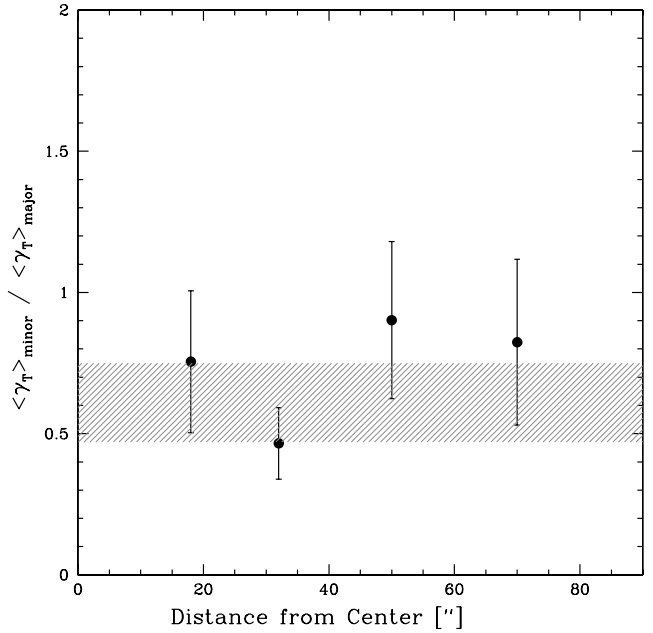

FIG. 11.—Same as Fig. 9, but for only lenses with axis ratios (b/a) between 0.5 and 0.8. This selection criterion will result in a lens sample that is dominated by early-type galaxies. The weighted average shear ratio is 0.61 ± 0.14.

by the contribution to the "one-halo" term from the matter distribution around the galaxy itself, rather than from the host halo of any satellite galaxies within groups or clusters.

A recent analysis of isolated galaxies in the SDSS indicated that the number density of satellite galaxies is higher near the major axes of a central galaxies than that near the minor axes (Brainerd 2005). This, together with the suggestion that satellites show a preference for radial alignment with their hosts (Agustsson & Brainerd 2006b), indicates that the measured flattening from galaxy-galaxy lensing may be underestimating the true halo flattening. The signal along the major axes will be suppressed by the intrinsic alignment of the satellites; thus, our measurements should be considered a lower limit on halo ellipticity. In order to quantify this effect, it would be interesting to measure the preferred alignment of satellite galaxies and its dependence on their position angle with respect to their host galaxy for a large sample of hosts and satellites. Galaxy-galaxy lensing measurements using redshift information can eliminate this potential contaminant, as well as identify a sample of isolated foreground galaxies to eliminate the influence of the group or cluster environment.

5. SUMMARY

We have used early i' data from the CFHTLS to detect a significant galaxy-galaxy lensing signal and to constrain the velocity dispersion of galaxy halos at a redshift of 0.3. The measured velocity dispersion for an L_* galaxy is 137 ± 11 km s^{-1} (corresponding to a circular velocity of $V_* = 194 \pm 15$ km s^{-1}). This result is consistent with previous galaxy-galaxy lensing estimates (Kleinheinrich et al. 2005; Hoekstra et al. 2005).

In addition, we were able to estimate the total mass of an L_* galaxy at redshift 0.3 to be $(2.2 \pm 0.4) \times 10^{12}\, h^{-1}\, M_\odot$, which corresponds to a virial mass, M_{200}, of $(1.1 \pm 0.2) \times 10^{12}\, h^{-1}\, M_\odot$. This is in good agreement with the results from the RCS (Hoekstra et al. 2005), the SDSS (Mandelbaum et al. 2006b), and the GEMS survey (Heymans et al. 2006b).

We also saw some evidence for nonspherical dark matter halos, although a definitive answer awaits more data. With multicolor data we will be able to repeat the anisotropic weak-lensing measurements for subsamples of lenses selected by color, morphology, and redshift. This will also allow a detailed comparison to the low-redshift results obtained by Mandelbaum et al. (2006b).

Galaxy-galaxy lensing is a unique and powerful tool with which to study the dark matter halos of galaxies to large projected distances. This technique has now been successfully applied to many different data sets, but with planned and ongoing major surveys the results will only improve. Any complete theory of galaxy formation must be able to properly map both the baryonic and the dark matter components of galaxies, and understanding which galaxies live in which halos is a major piece of this puzzle. Many observations can help in understanding the baryonic component of galaxies, while simulations are best at explaining the dark matter component. Gravitational lensing has an important role to play in uniting simulations and other observations by connecting galaxies to their halos.

There is clearly much more that can and will be done with the entire CFHTLS data set. In particular, having photometric redshifts will aid the analysis immensely. At present, we have lenses and sources over a wide range of redshifts and are estimating shear in angular bins that mix together many physical scales. Furthermore, photometric redshifts will permit a clear division between lens and source populations, rather than a statistical one based on observed magnitudes, such as that used here. This should help alleviate the concerns of intrinsic alignments. Redshift information will also permit the division of lenses into different redshift bins, thus allowing us to study halo evolution.

A further use of the photometric redshifts could be to create catalogs of isolated lens galaxies. If the lens sample includes both central galaxies and their satellites and the satellites are aligned with their host, then the galaxy-galaxy lensing signal could be biased. Also, the lensing signal around satellites will be influenced both by the dark matter halo of the satellite and by the central galaxy. This issue can be addressed by measuring the lensing around only around the isolated "central" galaxies or by attempting to measure the signal around the central and satellite galaxies separately (e.g., Hoekstra et al. 2005; Yang et al. 2006). It is also possible to model the satellite contribution to the lensing signal (e.g., Guzik & Seljak 2001).

We also plan to measure the morphologies of all of the lens galaxies so that we can divide the sample into early and late types and try to detect differences in their halo masses, shapes, and M/L ratios. Furthermore, with the complete data set we should have sufficient statistical power to be able to distinguish between dark matter profiles. For example, we should be able to tell whether the tangential shear is best fitted by an NFW profile (Navarro et al. 1996), an isothermal sphere profile, or a Moore profile (Moore et al. 1999).

We would like to thank Joel Primack and Tereasa Brainerd for helpful discussions. The authors would also like to thank the anonymous referee for a careful reading of the manuscript and many helpful suggestions that improved the paper.

This work is based on observations obtained with MegaPrime/MegaCam, a joint project of CFHT and CEA/DAPNIA, at the Canada-France-Hawaii Telescope (CFHT), which is operated by the National Research Council (NRC) of Canada, the Institut National des Science de l'Univers of the Centre National de la Recherche Scientifique (CNRS) of France, and the University of Hawaii. This work is based in part on data products produced at TERAPIX and the Canadian Astronomy Data Centre as part of the Canada-France-Hawaii Telescope Legacy Survey, a collaborative project of NRC and CNRS.

REFERENCES

Agustsson, I., & Brainerd, T. G. 2006a, ApJ, 644, L25
———. 2006b, ApJ, 650, 550
Alam, S. M. K., & Ryden, B. S. 2002, ApJ, 570, 610
Allgood, B., Flores, R. A., Primack, J. R., Kravtsov, A. V., Wechsler, R. H., Faltenbacher, A., & Bullock, J. S. 2006, MNRAS, 367, 1781
Astier, P., et al. 2006, A&A, 447, 31
Bartelmann, M. 1996, A&A, 313, 697
Bekenstein, J. D. 2004, Phys. Rev. D, 70, 083509
Bertin, E., & Arnouts, S. 1996, A&AS, 117, 393
Brainerd, T. G. 2005, ApJ, 628, L101
Brainerd, T. G., Blandford, R. D., & Smail, I. 1996, ApJ, 466, 623
Brainerd, T. G., & Wright, C. O. 2000, PASP, submitted (astro-ph/0006281)
Brown, M. L., Taylor, A. N., Bacon, D. J., Gray, M. E., Dye, S., Meisenheimer, K., & Wolf, C. 2003, MNRAS, 341, 100
Bullock, J. S., Kolatt, T. S., Sigad, Y., Somerville, R. S., Kravtsov, A. V., Klypin, A. A., Primack, J. R., & Dekel, A. 2001, MNRAS, 321, 559
Cohen, J. G., Hogg, D. W., Blandford, R., Cowie, L. L., Hu, E., Songaila, A., Shopbell, P., & Richberg, K. 2000, ApJ, 538, 29
Conroy, C., et al. 2005, ApJ, 635, 982
Davé, R., Spergel, D. N., Steinhardt, P. J., & Wandelt, B. D. 2001, ApJ, 547, 574
Dubinski, J., & Carlberg, R. G. 1991, ApJ, 378, 496
Faber, S. M., & Jackson, R. E. 1976, ApJ, 204, 668
Fernández-Soto, A., Lanzetta, K. M., & Yahil, A. 1999, ApJ, 513, 34
Frei, Z., & Gunn, J. E. 1994, AJ, 108, 1476
Guzik, J., & Seljak, U. 2001, MNRAS, 321, 439
Heymans, C., et al. 2006a, MNRAS, 368, 1323
———. 2006b, MNRAS, 371, L60
Hoekstra, H., Franx, M., & Kuijken, K. 2000, ApJ, 532, 88
Hoekstra, H., Franx, M., Kuijken, K., Carlberg, R., & Gladders, H. Y. 2003, MNRAS, 340, 609
Hoekstra, H., Franx, M., Kuijken, K., & Squires, G. 1998, ApJ, 504, 636
Hoekstra, H., Hsieh, B. C., Yee, H. K. C., Lin, H., & Gladders, M. D. 2005, ApJ, 635, 73
Hoekstra, H., Yee, H. K. C., & Gladders, M. D. 2004, ApJ, 606, 67
Hoekstra, H., Yee, H. K. C., Gladders, M. D., Barrientos, L. F., Hall, P. B., & Infante, L. 2002, ApJ, 572, 55
Hoekstra, H., et al. 2006, ApJ, 647, 116
Hudson, M. J., Gwyn, S. D. J., Dahle, H., & Kaiser, N. 1998, ApJ, 503, 531
Ilbert, O., et al. 2006, A&A, 457, 841
Kaiser, N., Squires, G., & Broadhurst, T. 1995, ApJ, 449, 460
Kleinheinrich, M., et al. 2005, A&A, 439, 513
Lin, H., Yee, H. K. C., Carlberg, R. G., Morris, S. L., Sawicki, M., Patton, D. R., Wirth, G., & Shepherd, C. W. 1999, ApJ, 518, 533
Mandelbaum, R., Hirata, C. M., Broderick, T., Seljak, U., & Brinkmann, J. 2006a, MNRAS, 370, 1008
Mandelbaum, R., Seljak, U., Kauffmann, G., Hirata, C. M., & Brinkmann, J. 2006b, MNRAS, 368, 715
Massey, R., et al. 2007, MNRAS, 376, 13
Milgrom, M. 2002, NewA Rev., 46, 741
Moore, B., Ghigna, S., Governato, F., Quinn, G. L. T., Stadel, J., & Tozzi, P. 1999, ApJ, 524, L19
Mortlock, D. J., & Turner, E. L. 2001, MNRAS, 327, 557
Natarajan, P., & Refregier, A. 2000, ApJ, 538, L113
Navarro, J. F., Frenk, C. S., & White, S. D. 1996, ApJ, 462, 563
Novak, G. S., Cox, T. J., Primack, J. R., Jonsson, P., & Dekel, A. 2006, ApJ, 646, L9
Prada, F., et al. 2003, ApJ, 598, 260
Schneider, P., & Rix, H.-W. 1997, ApJ, 474, 25
Sheldon, E. S., et al. 2004, AJ, 127, 2544
Sheth, R. K., et al. 2003, ApJ, 594, 225
Skordis, C., Mota, D. F., Ferreira, P. G., & Bœhm, C. 2006, Phys. Rev. Lett., 96, 011301
Springel, V., White, S. D. M., & Hernquist, L. 2004, in IAU Symp. 220, Dark Matter in Galaxies, ed. S. D. Ryder, D. J. Pisano, M. A. Walker, & K. C. Freeman (San Francisco: ASP), 421
van Waerbeke, L., White, M., Hoekstra, H., & Heymans, C. 2006, Astropart. Phys., 26, 91
Wright, C. O., & Brainerd, T. G. 2000, ApJ, 534, 34
Yang, X., Mo, H. J., van den Bosch, F. C., Jing, Y. P., Weinmann, S. M., & Meneghetti, M. 2006, MNRAS, 373, 1159
Yee, H., et al. 2000, ApJS, 129, 475
Yoo, J., Tinker, J. L., Weinberg, D. H., Zheng, Z., Katz, N., & Davé, R. 2006, ApJ, 652, 26
Zaritsky, D., & White, S. D. M. 1994, ApJ, 435, 599
Zehavi, I., et al. 2004, ApJ, 608, 16
Zhao, H., Bacon, D. J., Taylor, A. N., & Horne, K. 2006, MNRAS, 368, 171